Draft version April 18, 2023
Preprint typeset using LaTeX style emulateapj v. 12/16/11

PROBING THE SOLAR INTERIOR WITH LENSED GRAVITATIONAL WAVES FROM KNOWN PULSARS

Ryuichi Takahashi[1], Soichiro Morisaki[2] and Teruaki Suyama[3]
[1] Faculty of Science and Technology, Hirosaki University, 3 Bunkyo-cho, Hirosaki, Aomori 036-8561, Japan
[2] Institute for Cosmic Ray Research (ICRR), KAGRA Observatory, The University of Tokyo, Kashiwa City, Chiba 277-8582, Japan
[3] Department of Physics, Tokyo Institute of Technology, 2-12-1 Ookayama, Meguro-ku, Tokyo 152-8551, Japan
Draft version April 18, 2023

ABSTRACT

When gravitational waves (GWs) from a spinning neutron star arrive from behind the Sun, they are subjected to gravitational lensing that imprints a frequency-dependent modulation on the waveform. This modulation traces the projected solar density and gravitational potential along the path as the Sun passes in front of the neutron star. We calculate how accurately the solar density profile can be extracted from the lensed GWs using a Fisher analysis. For this purpose, we selected three promising candidates (the highly spinning pulsars J1022+1001, J1730-2304, and J1745-23) from the pulsar catalog of the Australia Telescope National Facility. The lensing signature can be measured with 3σ confidence when the signal-to-noise ratio (SNR) of the GW detection reaches $100\,(f/300\mathrm{Hz})^{-1}$ over a one-year observation period (where f is the GW frequency). The solar density profile can be plotted as a function of radius when the SNR improves to $\gtrsim 10^4$.

Subject headings: gravitational lensing: weak — gravitational waves — Sun: general

1. INTRODUCTION

Since the direct detection of gravitational wave (GW) signal from a merging black hole binary (GW150914: Abbott et al. 2016), GW astronomy has attracted increasing interest. Currently, all GW sources detected by the ground-based detectors of the Laser Interferometer Gravitational-Wave Observatory (LIGO), the Virgo interferometer, and the Kamioka Gravitational Wave Detector (KAGRA) are compact binary coalescences (CBCs) of stellar-mass black holes and neutron stars. The LIGO-Virgo-KAGRA (LVK) collaboration reported ~ 90 candidates of CBC events (The LIGO Scientific Collaboration et al. 2021). However, the ground-based detectors are also expected to detect spinning neutron stars (e.g., Abbott et al. 2022b). A neutron star that is non-axisymmetric around its spin axis, resulting in a so-called mountainous profile, emits continuous GWs. Non-axisymmetry may be caused by crustal deformation, magnetic fields, and mass accretion from the star's companion (e.g., recent reviews by Glampedakis & Gualtieri (2018) and Riles (2022)). Although the LVK collaboration has been searching for continuous GW signals, no event has yet been reported (Abbott et al. 2021, 2022b,a; The LIGO Scientific Collaboration et al. 2022).

If a GW signal encounters the Sun along its path, gravitational lensing imprints a frequency-dependent modulation on the waveform. In geometrical optics (i.e., the zero wavelength limit of GWs), the solar density modulates the amplitude with a magnification effect, while the gravitational potential modulates the phase by imposing a potential (or Shapiro) time delay. These modulations can be obtained along the transversal path of the Sun moving in front of the source (the duration of this movement is approximately half a day). Therefore, in principle, one can probe the solar interior using the lensed signal. GW lensing by the Sun has been studied as a tool for amplifying the strain amplitudes of GWs from a distant source and probing the solar structure (e.g., Cyranski & Lubkin 1974; Sonnabend 1979; Patla & Nemiroff 2008; Marchant et al. 2020). Before the 1980s, these studies were based on geometrical optics. Bontz & Haugan (1981) first demonstrated that the diffraction effect caused by the finite wavelength of GWs suppresses magnification near the focal point at lower frequencies ($f \lesssim 10^4\,\mathrm{Hz}$). Recently, Marchant et al. (2020) proposed that the solar structure can be probed through the lensed GW signals from a pulsar behind the Sun. However, they only roughly estimated the detectability of the lensing signature, without calculating the measurement accuracy of the density profile. Very recently, Jung & Kim (2022) reported that the Fresnel scale is comparable to the solar radius within the frequency band of the ground-based detectors; therefore, the inner profile of the Sun can (in principle) be probed with the lensing modulation on a chirp signal from a CBC.

In this study, we investigated the accuracy of measuring the solar density profile using the lensed signal of a known pulsar. Because ground-based detectors detect GW wavelengths longer than (or comparable to) the solar Schwarzschild radius, gravitational lensing should employ wave optics (e.g., Ohanian 1974; Bliokh & Minakov 1975; Schneider et al. 1992; Nakamura & Deguchi 1999; Takahashi & Nakamura 2003; Dai et al. 2018; Oguri 2019; Liao et al. 2022). We first calculate the lensed waveform based on wave optics. We discuss the effects of frequency and impact parameter on the waveform (Section 2). Then, we extracted the known pulsars crossing behind the Sun from the Australia Telescope National Facility (ATNF) pulsar catalog (Manchester et al. 2005). From the extracted list, we select suitable candidates by calculating the lensing modulations of these pulsars (Section 3). Using these candidates, we calculate the detectability of the lensing signature and the accuracy of measuring the solar density profile through a Fisher analysis (Section 4). Finally, we roughly estimate the number of Galactic millisecond pulsars (MSPs) behind the Sun, which are potentially detectable by near-future radio sur-

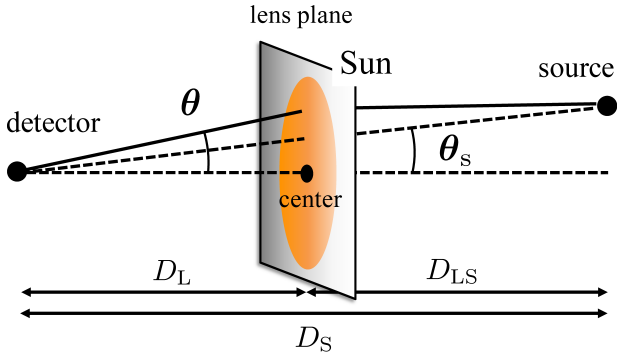

FIG. 1.— Configuration of the detector, Sun, and source. $D_{\rm L}$, $D_{\rm LS}$, and $D_{\rm S}$ denote the distances between them. Solid line is the GW path. Angular coordinates $\boldsymbol{\theta}$ and $\boldsymbol{\theta}_{\rm s}$ describe the incoming direction of the GWs and source position, respectively, with respect to the solar center.

veys (Section 5). The study findings are summarized in Section 6.

2. AMPLITUDE AND PHASE MODULATIONS OF SOLAR LENSING

This section introduces amplitude and phase modulations of lensed waveform, based on wave optics.

2.1. *Lensed waveform*

Figure 1 shows the configuration of the detector, Sun, and source. The solid line describes a single GW path[1]. We assume the thin-lens approximation, in which the solar density and its gravitational potential are projected onto a plane perpendicular to the line-of-sight. Furthermore, we assume the flat-sky approximation, in which $|\boldsymbol{\theta}|, |\boldsymbol{\theta}_{\rm s}| \ll 1$. As the coordinate system is fixed at the solar position, the background source (pulsar) moves along the ecliptic longitude following the annual solar motion. The distance to the Sun is $D_{\rm L} = 1\,{\rm au}$ and the solar angular radius is $\theta_\odot = \arctan[R_\odot/(1\,{\rm au})] \simeq 16$ arcmin. In this paper, the annual modulation of $D_{\rm L}$ is ignored because it changes by $< 2\,\%$ as the Earth moves elliptically around the Sun.

The lensed waveform $\tilde{h}^{\rm L}(f)$ in the frequency domain is obtained by multiplying the unlensed waveform $\tilde{h}(f)$ by a function $F(f;\boldsymbol{\theta}_{\rm s})$ (e.g., Nakamura 1998; Takahashi & Nakamura 2003):

$$\begin{aligned}\tilde{h}^{\rm L}(f;\boldsymbol{\theta}_{\rm s}) &= F(f;\boldsymbol{\theta}_{\rm s})\tilde{h}(f),\\ &= [1 + A_F(f;\boldsymbol{\theta}_{\rm s})]\,{\rm e}^{{\rm i}\Phi_F(f;\boldsymbol{\theta}_{\rm s})}\tilde{h}(f). \end{aligned} \quad (1)$$

In the second line, A_F ($\equiv |F| - 1$) and Φ_F ($\equiv \ln(F/|F|)$) represent the amplitude and phase modulations, respectively. The GW polarization is ignored because the polarization rotation due to lensing is negligibly small (e.g., Hou et al. 2019; Ezquiaga et al. 2021; Dalang et al. 2022). The function F, called the amplification factor or transmission factor, is given by the following diffraction integral (e.g., Schneider et al. 1992):

$$F(f;\boldsymbol{\theta}_{\rm s}) = \frac{D_{\rm L}D_{\rm S}}{cD_{\rm LS}}\frac{f}{\rm i}\int {\rm d}^2\theta \exp\left[2\pi {\rm i} f t_{\rm d}(\boldsymbol{\theta},\boldsymbol{\theta}_{\rm s})\right], \quad (2)$$

[1] In wave optics, the lensed waveform is the superposition of many GW paths from the source to the detector (Eq. (2)). The solid line represents one of them.

where the time delay is given by

$$t_{\rm d}(\boldsymbol{\theta},\boldsymbol{\theta}_{\rm s}) = \frac{1}{c}\left[\frac{D_{\rm L}D_{\rm S}}{2D_{\rm LS}}|\boldsymbol{\theta} - \boldsymbol{\theta}_{\rm s}|^2 - \frac{\hat{\psi}(\boldsymbol{\theta})}{c^2}\right]. \quad (3)$$

The first and second terms are the geometrical and potential (or Shapiro) time delays, respectively. Because the distance to the Sun is much shorter than the distance to the source, hereafter, we assume that $D_{\rm S}/D_{\rm LS} \simeq 1$. The two-dimensional lens potential $\hat{\psi}(\boldsymbol{\theta})$ is determined from the solar-projected density profile $\Sigma(\boldsymbol{\theta})$ using the Poisson equation:

$$\nabla_\theta^2\hat{\psi}(\boldsymbol{\theta}) = 8\pi G D_{\rm L}^2\Sigma(\boldsymbol{\theta}). \quad (4)$$

Outside the Sun, the potential is identical to that of a point mass:

$$\hat{\psi}(\theta) = 4GM_\odot \ln\left(\frac{\theta}{\theta_{\rm E}}\right) \quad \text{for } \theta > \theta_\odot, \quad (5)$$

where $\theta_{\rm E}$ is an arbitrary constant, here set to the angular Einstein radius; i.e., $\theta_{\rm E} = [4GM_\odot/(c^2D_{\rm L})]^{1/2} \simeq 0.043\,\theta_\odot$. The Sun is modeled using the BS05(OP) spherical density model[2] in Bahcall et al. (2005). The model density agrees within 2 % of the helioseismological results across the whole radius (their Fig. 1). As the density profile is spherical, the integration (2) can be performed over the azimuth and F reduces to

$$\begin{aligned}F(f;\theta_{\rm s}) = \frac{2\pi f D_{\rm L}}{{\rm i}c}\int_0^\infty {\rm d}\theta\,\theta J_0\left(\frac{2\pi f D_{\rm L}}{c}\theta\theta_{\rm s}\right)\\ \times \exp\left[2\pi {\rm i} f\left\{\frac{1}{2c}D_{\rm L}\left(\theta^2 + \theta_{\rm s}^2\right) - \frac{\hat{\psi}(\theta)}{c^3}\right\}\right], \end{aligned} \quad (6)$$

where J_0 is the zero order Bessel function. Equation (6) is numerically integrated using integration by parts (Appendix A of Takahashi (2004); Guo & Lu (2020)).

2.2. *High- and low-frequency limits*

This subsection presents the high- and low-frequency limits of the amplification factor. In the high-frequency limit (i.e., the geometrical-optics limit), because the exponential term of F in Eq. (2) oscillates violently, a stationary point of $t_{\rm d}(\boldsymbol{\theta},\boldsymbol{\theta}_{\rm s})$ contributes to the integral (e.g., Schneider et al. 1992). This point is a solution of $\nabla_\theta t_{\rm d}(\boldsymbol{\theta},\boldsymbol{\theta}_{\rm s}) = 0$:

$$\boldsymbol{\theta}_{\rm s} = \boldsymbol{\theta} - \hat{\boldsymbol{\alpha}}(\boldsymbol{\theta}), \quad (7)$$

from Eq. (3), where $\hat{\boldsymbol{\alpha}} = \nabla_\theta\hat{\psi}/(c^2D_{\rm L})$ is the deflection angle. Equation (7) is the lens equation. The image position $\boldsymbol{\theta}_{\rm i}$ is obtained by solving Eq. (7). Note that only a single image is formed irrespective of $\boldsymbol{\theta}_{\rm s}$. In the high-frequency limit, F reduces to the following simple form:

$$\lim_{f\to\infty} F(f;\boldsymbol{\theta}_{\rm s}) = |\mu(\boldsymbol{\theta}_{\rm i},\boldsymbol{\theta}_{\rm s})|^{1/2}\exp\left[2\pi i f t_{\rm d}(\boldsymbol{\theta}_{\rm i},\boldsymbol{\theta}_{\rm s})\right], \quad (8)$$

where $\mu = [\det(\partial\boldsymbol{\theta}_{\rm s}/\partial\boldsymbol{\theta}_{\rm i})]^{-1}$ is the magnification of the image.

[2] The numerical table can be downloaded from http://www.sns.ias.edu/ jnb/SNdata/sndata.html#bs2005.

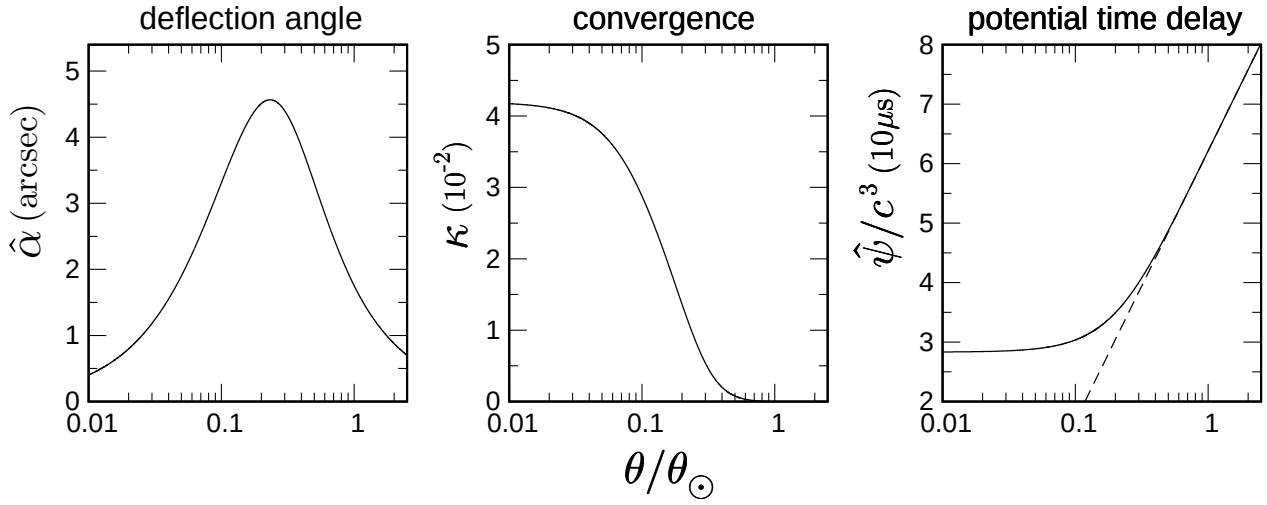

FIG. 2.— Solar deflection angle, convergence, and potential (or Shapiro) time delay as functions of angular radius θ (normalized by the solar radius $\theta_\odot$). The convergence κ in the middle panel is the dimensionless projected density profile. The potential time delay in the right panel is the projected gravitational potential divided by c^3. Near and outside the surface ($\theta/\theta_\odot \gtrsim 1$), the result approaches that of Eq. (5) for a point mass (the dashed line).

In the weak-gravitational field limit, the magnification can be approximated as $\mu \simeq 1 + 2\kappa$, where $\kappa = \Sigma/\Sigma_{\rm cr}$ is the convergence and $\Sigma_{\rm cr} = c^2/(4\pi G D_{\rm L})$ is the critical density (e.g., Bartelmann & Schneider 2001). Accordingly, A_F and Φ_F reduce to

$$\lim_{f\to\infty} A_F(f;\boldsymbol{\theta}_{\rm s}) \simeq \kappa(\boldsymbol{\theta}_{\rm s}) = \frac{4\pi G D_{\rm L}}{c^2}\Sigma(\boldsymbol{\theta}_{\rm s}),$$
$$\lim_{f\to\infty} \Phi_F(f;\boldsymbol{\theta}_{\rm s}) = 2\pi f t_{\rm d}(\boldsymbol{\theta}_{\rm i},\boldsymbol{\theta}_{\rm s}) \simeq -2\pi f \frac{\hat{\psi}(\boldsymbol{\theta}_{\rm s})}{c^3}. \quad (9)$$

Therefore, A_F and Φ_F trace the projected density profile and gravitational potential, respectively.

Figure 2 plots the deflection angle, convergence, and gravitational potential as functions of θ (as these variables are functions of θ, we plot θ rather than $\theta_{\rm s}$ along the x-axis). The deflection angle is consistent with the known result $\hat{\alpha} = 4GM_\odot/(c^2 R_\odot) \simeq 1.75\,$arcsec at the surface. The maximum deflection is $\hat{\alpha} \simeq 4.57\,$arcsec at $\theta \simeq 0.23\,\theta_\odot$. Because $\hat{\alpha}$ is much smaller than the solar radius ($\theta_\odot \simeq 16\,$arcmin), we can safely set $\boldsymbol{\theta}_{\rm i} \simeq \boldsymbol{\theta}_{\rm s}$ from Eq. (7). Therefore, the second term of $t_{\rm d}$ in Eq. (3) exceeds the first term in the geometrical-optics limit. Meanwhile, the convergence κ is maximized at ~ 0.04 near the center. The profile is flat at the core ($\theta \lesssim 0.03\,\theta_\odot$), but it drops steeply at $\theta \gtrsim 0.1\,\theta_\odot$. The typical gravitational time delay is $\approx 10^{-5}$ s in the Sun. Near the center, the potential in Eq. (4) can be approximated as $\hat{\psi}(\theta) = \text{ const.} + (c^2 D_{\rm L}/2)\,\kappa(\theta=0)\,\theta^2 + \mathcal{O}(\theta^3)$. The results of Fig. 2 are consistent with previous works on lensing by the transparent Sun (Bontz & Haugan 1981; Patla & Nemiroff 2008; Marchant et al. 2020; Jung & Kim 2022).

In the large-angle limit $\theta_{\rm s} \gg \theta_\odot$, the geometrical-optics result (9) is recovered because $2\pi f t_{\rm d} \gg 1$. As the gravitational potential in Eq. (5) is valid only for $\theta \ll 1$, it must be replaced with (e.g., Backer & Hellings 1986)

$$\hat{\psi}(\theta) = 2GM_\odot \ln\left\{\frac{2(1-\cos\theta)}{\theta_{\rm E}^2}\right\}, \quad (10)$$

when $\theta \gtrsim 1$.

We now investigate the low-frequency limit. Changing the variables to $\boldsymbol{\theta}' = \sqrt{f}\boldsymbol{\theta}$ and $\boldsymbol{\theta}'_{\rm s} = \sqrt{f}\boldsymbol{\theta}_{\rm s}$ in Eq. (2), F is rewritten as

$$F(f;\boldsymbol{\theta}_{\rm s}) = \frac{D_{\rm L}}{{\rm i}c}\int {\rm d}^2\boldsymbol{\theta}' \exp\left[\frac{2\pi{\rm i}}{c}\left\{\frac{D_{\rm L}}{2}\left|\boldsymbol{\theta}' - \boldsymbol{\theta}'_{\rm s}\right|^2 - \frac{f}{c^2}\hat{\psi}\left(\frac{\boldsymbol{\theta}'}{\sqrt{f}}\right)\right\}\right]. \quad (11)$$

In the low-frequency limit, $\hat{\psi}$ can be replaced with its value at infinity:

$$\lim_{f\to 0}\hat{\psi}\left(\frac{\theta'}{\sqrt{f}}\right) = 4GM_\odot \ln\left(\frac{\theta'}{\sqrt{f}\theta_{\rm E}}\right),$$

from Eq. (5). Inserting this $\hat{\psi}$ into Eq. (11) and expanding f as a Taylor series, we have

$$\lim_{f\to 0} A_F(f;\boldsymbol{\theta}_{\rm s}) = \frac{2\pi^2 GM_\odot}{c^3}f,$$
$$\lim_{f\to 0} \Phi_F(f;\boldsymbol{\theta}_{\rm s}) = \frac{4\pi GM_\odot}{c^3}f\left[\gamma + \ln\left(\frac{4\pi GM_\odot}{c^3}f\right)\right], \quad (12)$$

where $\gamma = 0.5772\cdots$ is Euler's constant.

2.3. *Amplitude and phase modulations*

Figure 3 plots A_F and Φ_F as functions of f for various $\theta_{\rm s}$. In the high- and low-frequency limits, the plots are consistent with the analytical results of Eqs. (9) and

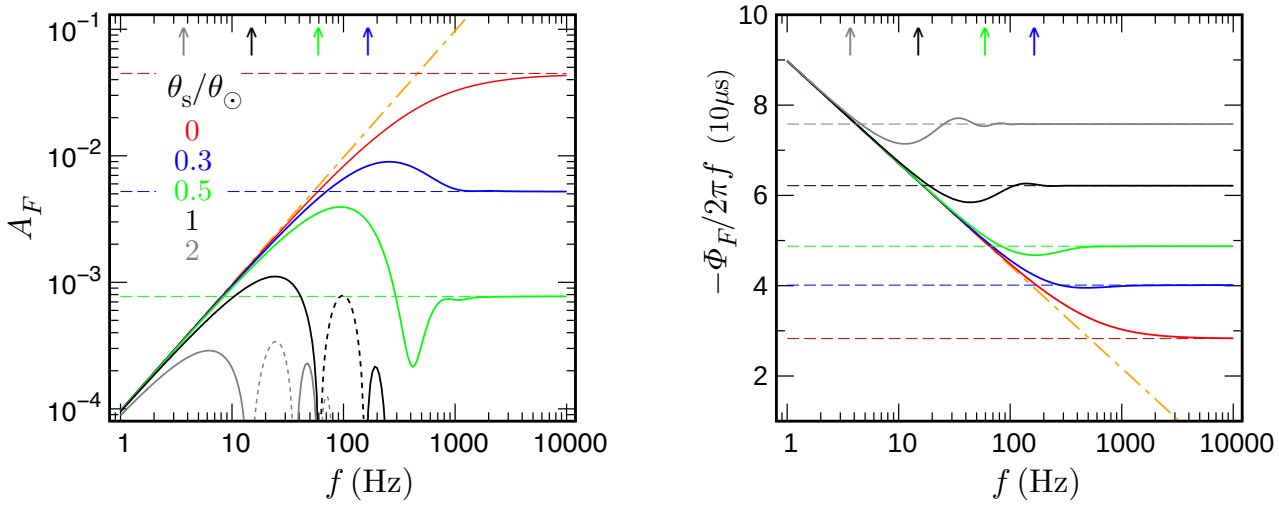

FIG. 3.— Amplitude and phase modulations as functions of frequency at various source positions $\theta_s/\theta_\odot = 0$–2. Horizontal dashed lines and dot-dashed orange lines represent the analytical results in the high- and low-frequency limits, respectively, given by Eqs. (9) and (12). Up arrows indicate the rough boundary between the wave- and geometrical-optics regions for each θ_s (the description after Eq. (13) in the text). In the left panel, dotted curves denote negative values ($A_F < 0$). In the right panel, the phase modulation is divided by $2\pi f$, which corresponds to an arrival time delay.

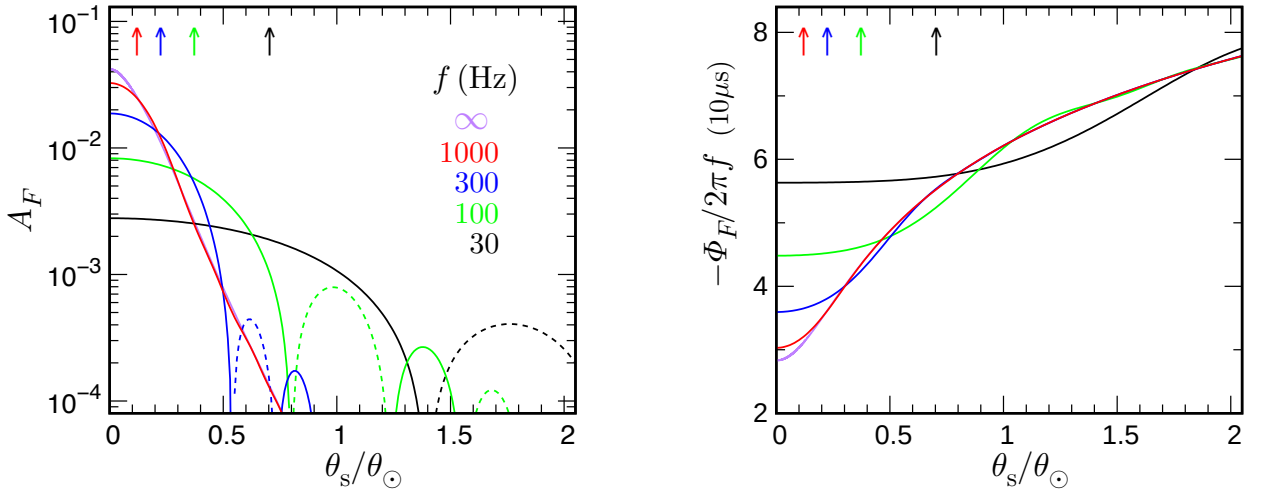

FIG. 4.— Same as Fig.3, but plotted as functions of $\theta_s/\theta_\odot$ for various f. Red curve overlaps the purple curve (representing the high-frequency limit) everywhere except near the center ($\theta_s/\theta_\odot \lesssim 0.2$).

(12), respectively. As the frequency of a chirp signal from an inspiral binary sweeps from low to high, A_F increases proportionally to f in the wave-optics regime but approaches a constant value of κ in Eq. (9) in the geometrical-optics regime. Similarly, $-\Phi_F/(2\pi f)$ decreases logarithmically but approaches a constant value of the potential time delay ($\hat{\psi}/c^3$). These modulations are observed even outside the Sun ($\theta_s = 2\theta_\odot$). Therefore, within the frequency range of ground-based detectors, the solar lensing imprints unique frequency-dependent modulations on both the amplitude and phase. The solar structure can (in principle) be extracted from the chirp signal (recent study by Jung & Kim 2022). However, in the high-frequency limit, solar structure extraction from the signal (even from a chirp signal) is impossible at fixed θ_s because the constant A_F is degenerate with an intrinsic amplitude of GWs. Similarly, the constants Φ_F and $\Phi_F/(2\pi f)$ are degenerate with an intrinsic phase and arrival time, respectively. Therefore, in geometrical optics, the lensing modulations are indistinguishable from the intrinsic source properties (unless lensed signals with various θ_s are available). Figure 3 is consistent with Fig. 2 of Jung & Kim (2022).

To discuss the behavior of these modulations in more detail, let us introduce the angular Fresnel scale (Macquart 2004; Takahashi 2006):

$$\theta_F = \left(\frac{c}{2\pi f}\frac{1}{D_L}\right)^{1/2}, \simeq 0.38\,\theta_\odot \left(\frac{f}{100\,\mathrm{Hz}}\right)^{-1/2}. \quad (13)$$

In the low-frequency limit, the lensed signal probes a circle of radius θ_F around the source position (Section 2 and Fig. 1 of Choi et al. 2021). In other words, the Fresnel scale can be interpreted as the effective source

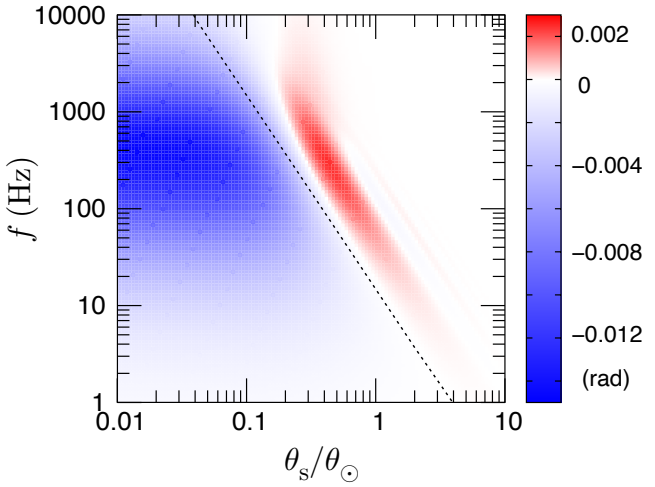

FIG. 5.— Contour plot of the difference between the phase modulation and its geometrical-optics limit ($\Phi_F - 2\pi f t_d$). Red, blue, and white regions correspond to positive, negative, and zero differences, respectively. Dotted line plots the rough boundary between the wave- and geometrical-optics regions, calculated from $\theta_F = \theta_s$ (the description after Eq. (13) in the text).

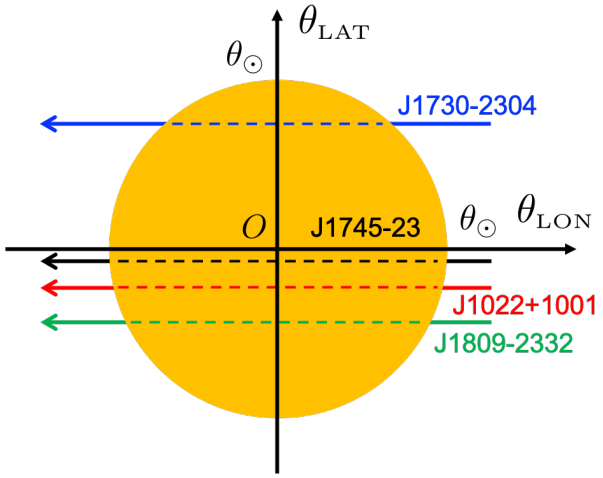

FIG. 6.— Trajectories of pulsars moving behind the Sun (represented by an orange circle of radius $\theta_\odot$). θ_{LAT} is the ecliptic latitude and θ_{LON} is the ecliptic longitude with origin set at the solar center.

radius (Oguri & Takahashi 2020). The effective source radius shrinks with increasing f in the chirp signal. In the high-frequency limit, the lensing probes a small region around the image position. As the modulations at different f can probe different regions, one can in principle probe the density profile (Jung & Kim 2022). Here, $\theta_F = \theta_s$ (unless $\theta_s = 0$) roughly represents the boundary between the wave- and geometrical-optics regions. This boundary condition is derived from $2\pi f t_d = 1$ with neglecting the potential term in Eq. (3) (Section II.B of Choi et al. (2021) and Section 3 of Jung & Kim (2022))[3]. The boundary is plotted as a series of up arrows in Figs. 3 and 4.

Figure 4 plots A_F and Φ_F as functions of θ_s for various fixed f. As the GWs from a pulsar are continuous, one can (in principle) measure A_F and Φ_F as functions of θ_s for a pulsar moving behind the Sun. For smaller (larger) θ_s, the exponential term of the amplification factor ($= 2\pi f t_d$) is smaller (larger) and the results approach the low-frequency (high-frequency) limit in Eq. (12) (Eq. (9)). At $f = 1000$ Hz, the result almost matches that of geometrical optics except in the near-center region ($\theta_s/\theta_\odot \lesssim 0.2$). As Φ_F reflects the gravitational potential, it can be measured even outside the Sun. However, A_F, which reflects the mass density, falls steeply near the surface. Figure 4 is consistent with Figs. 6 and 7 of Marchant et al. (2020).

The LVK analysis accounts for the Shapiro time delay imposed by the Sun. In searches of continuous GWs (Abbott et al. 2017, 2019, 2022b), the time delay has been calculated using the `TEMPO` (Nice et al. 2015) and `TEMPO2` (Edwards et al. 2006; Hobbs et al. 2006) packages developed for timing analyses of pulsar radio signals. However, as shown in Figs. 3 and 4, the Shapiro time delay is less accurate at lower f and smaller θ_s. To clarify the accuracy of the Shapiro time delay, Fig. 5 plots a contour map of the differences between the phase modulation and its geometrical-optics limit. The difference ranges from -0.015 to 0.002 rad and is most significant at $f \simeq 100$–1000 Hz near the center ($\theta_s \lesssim 0.2\,\theta_\odot$). At a lower frequencies ($f \lesssim 10$ Hz), the difference reduces because both Φ_F and $2\pi f t_d$ are proportional to f. As expected, the Shapiro time delay is recovered at high f or large θ_s. The dotted line, predicted by setting $\theta_F = \theta_s$, is apparently consistent with the boundary. Although the Shapiro time delay is less accurate inside the Sun, the error is small (0.015 rad at most).

3. KNOWN PULSARS

This section describes some known pulsars moving behind the Sun. From the results in Subsection 2.3, a pulsar with higher frequency and a smaller impact parameter to the Sun is more suitable for probing the solar structure. We searched the ATNF pulsar catalog[4] for pulsars satisfying the following criteria: i) $f > 10$ Hz and ii) closest distance to the solar center is within $3\,\theta_\odot$. Twelve samples met the criteria: four pulsars crossing behind the Sun and eight pulsars passing near but not behind the solar surface. The information of these pulsars is summarized in Table 1. The GW frequency f is twice the spin frequency for the GW emission from mass-quadrupole moment. These frequencies are covered by the sensitivity range of the current ground-based detectors. The LVK collaboration obtained 95% credible upper limits on the strain amplitudes of some of these samples from the O2 and O3 runs (Abbott et al. 2022b). They also presented the corresponding upper bounds on the ellipticity of the mass distribution (estimated from Eq. (15)). The collaboration also performed an all-sky search for continuous GWs coming from any (known and unknown) spinning neutron stars in isolated and binary systems (Abbott et al. 2021; The LIGO Scientific Collaboration et al. 2022). Their upper bound was $h_0^{95\%} \sim 1.1\,(2.0) \times 10^{-25}$ at $f = 100$–200 (50–700) Hz for isolated systems (and similarly for binary systems).

[3] This condition can also be derived from the intersection of the low- and high-frequency limits of the phase modulation. Setting $\lim_{f\to 0} \Phi_F = \lim_{f\to\infty} \Phi_F$ in Eqs. (9) and (12) with the point-mass potential (5) (which is valid only for $\theta_s \gtrsim 0.3\,\theta_\odot$ in the right panel of Fig. 2), one obtains $\theta_F \simeq 0.94\,\theta_s$.

[4] http://www.atnf.csiro.au/research/pulsar/psrcat/

TABLE 1
PULSARS WITH $f > 10\,\mathrm{Hz}$ CROSSING BEHIND THE SUN (UPPER FOUR) AND CLOSE TO, BUT NOT BEHIND, THE SUN (LOWER EIGHT)

name	f (Hz)	$\theta_{\rm LAT}/\theta_\odot$	$D_{\rm s}$ (kpc)	$h_0^{95\%}$	$\epsilon^{95\%}$	refs
J1745−23	369	−0.07	7.94	——	——	C20
J1022+1001	122	−0.24	0.64	7.7×10^{-27}	3.2×10^{-7}	C96,R21
J1809−2332	14	−0.45	0.88	——	——	A09,R11
J1730−2304	246	0.71	0.47	5.0×10^{-27}	3.7×10^{-8}	L95,R21
J1858-2216	839	1.80	0.92	7.8×10^{-27}	9.6×10^{-9}	S16
J1142+0119	394	−1.84	2.17	7.4×10^{-27}	9.8×10^{-8}	S16
J2310-0555	766	−1.99	1.56	——	——	S16
J1756-2251	70	2.14	0.73	6.1×10^{-27}	8.6×10^{-7}	F04,F14
J1646-2142	342	2.44	0.97	——	——	R12,R13
J1811-2405	752	−2.52	1.83	1.5×10^{-26}	4.5×10^{-8}	K10,N20
J1836-2354B	619	−2.74	3.20	——	——	L11
J1836-2354A	596	−2.78	3.20	——	——	L11

NOTE. — Second column: GW frequency. Third column: ecliptic latitude $\theta_{\rm LAT}$ (i.e., the minimum angular separation to the solar center). Pulsars are listed in order of increasing $|\theta_{\rm LAT}|$. Fourth column: distance $D_{\rm s}$, measured by parallax for J1022+1001, J1730-2304, and J1756-2251 and estimated from the dispersion measures with the Galactic free-electron distribution model YMW16 (Yao et al. 2017) for the other pulsars. Fifth and sixth columns: 95% upper limits on the strain amplitude and ellipticity, respectively, taken from the LVK results (Abbott et al. 2022b). Last column: references A09 (Abdo et al. 2009), C20 (Cameron et al. 2020), C96 (Camilo et al. 1996), F04 (Faulkner et al. 2004), F14 (Ferdman et al. 2014), K10 (Keith et al. 2010), L95 (Lorimer et al. 1995), L11 (Lynch et al. 2011), N20 (Ng et al. 2020), R11 (Ray et al. 2011), R12 (Ray et al. 2012), R21 (Reardon et al. 2021), R16 (Roy & Bhattacharyya 2013), and S16 (Sanpa-Arsa 2016).

Figure 6 shows the trajectories of the upper four pulsars in Table 1. These pulsars move along the horizontal axis with a velocity of $\dot\theta_{\rm LON} \simeq -2\pi/(1\mathrm{yr}) = -2.5\,\mathrm{arcmin/hour} = -0.15\,\theta_\odot/\mathrm{hour}$. The typical crossing time is $2\theta_\odot/|\dot\theta_{\rm LON}| \simeq 13\,\mathrm{hours}$. Marchant et al. (2020) included J1022+1001 and J1730-2304 as candidates but excluded the very recently discovered pulsar J1745-23 (Cameron et al. 2020).

Figure 7 plots A_F and Φ_F as functions of $\theta_{\rm LON}$ for the four pulsars. J1745-23, with the highest frequency and closest impact parameter, yields the maximum A_F ($\sim 2\,\%$). The highest $|\Phi_F|$ is $\sim 0.1\,\mathrm{rad}$ for all pulsars except J1809-2332. The anomalous result for J1809-2332 is attributable to the low frequency (14 Hz) of this pulsar. The typical $|\Phi_F|$ is estimated as $|\Phi_F| \simeq 2\pi f|t_{\rm d}| \simeq 0.1\,(f/200\,\mathrm{Hz})\,(|t_{\rm d}|/100\,\mu\mathrm{s})$. The right panel clearly shows the solar potential well around $\theta_{\rm LON}=0$. The effect is especially noticeable in the curves of J1745-23 and J1022+1001. As evidenced in the figure, $|A_F| \ll |\Phi_F|$.

Figure 8 plots Φ_F as a function of $\theta_{\rm LON}$ for the lower eight pulsars in Table 1. Because these pulsars (except for J1756-2251) have relatively high frequencies, their $|\Phi_F|$ are relatively large (> 0.1 rad). As these pulsars do not pass behind the Sun, their $|A_F|$ are negligibly small.

4. PARAMETER EXTRACTION FROM THE LENSED WAVEFORM

This section evaluates the accuracy to which the solar density profile can be extracted from the lensed GW signal through a Fisher analysis.

4.1. *Fisher matrix analysis*

We consider a highly spinning neutron star with a small non-axisymmetry around the spin axis as the GW source. Neglecting spin down, the source is assumed to emit continuous monochromatic GWs during the observational period. A waveform of frequency f is then described as

$$h(t;f) = h_0 \cos\left(2\pi f t + \phi_0\right), \tag{14}$$

where ϕ_0 is a constant phase. The strain amplitude h_0 is determined by the non-axisymmetry as (e.g., Riles 2022)

$$h_0 = \frac{4\pi^2 \epsilon G I f^2}{c^4 D_{\rm s}}, \tag{15}$$

where I is the moment of inertia about the spin axis and ϵ is the ellipticity of the moment of inertia. A gravitationally lensed waveform $h^{\rm L}(t;f)$ can be obtained from Eqs. (1) and (14) as[5]

$$h^{\rm L}(t;f) = h_0\left[1 + A_F(t;f)\right]\cos\left[2\pi f t + \phi_0 + \Phi_F(t;f)\right]. \tag{16}$$

Here, A_F and Φ_F are numerically obtained from Eqs. (1) and (6). When $\theta_{\rm s}$ is large ($\theta_{\rm s} > 20\,\theta_\odot$), we can apply the geometrical-optics results (Eqs. (9) and (10)), which are fully valid at such large angles (Fig. 4).

Suppose that the pulsar is observed from time $t = -T/2$ to $T/2$, where T is the observational period and $t=0$ is the time at which the pulsar is closest to the solar center. The signal-to-noise ratio (SNR) is calculated as

$$\begin{aligned}\mathrm{SNR}^2 &= \frac{1}{S_n(f)}\int_{-T/2}^{T/2} dt\left[h^{\rm L}(t;f)\right]^2, \\ &\simeq \frac{h_0^2}{2S_n(f)}\,T,\end{aligned} \tag{17}$$

where S_n is the noise spectrum of the detector. Throughout this paper, the measurement accuracies of the fitting

[5] Here, we perform a Fourier transform to obtain the unlensed waveform in the frequency domain, then calculate the lensed waveform using Eq. (1), and finally repeat the Fourier transform to obtain the lensed waveform (16) in the time domain.

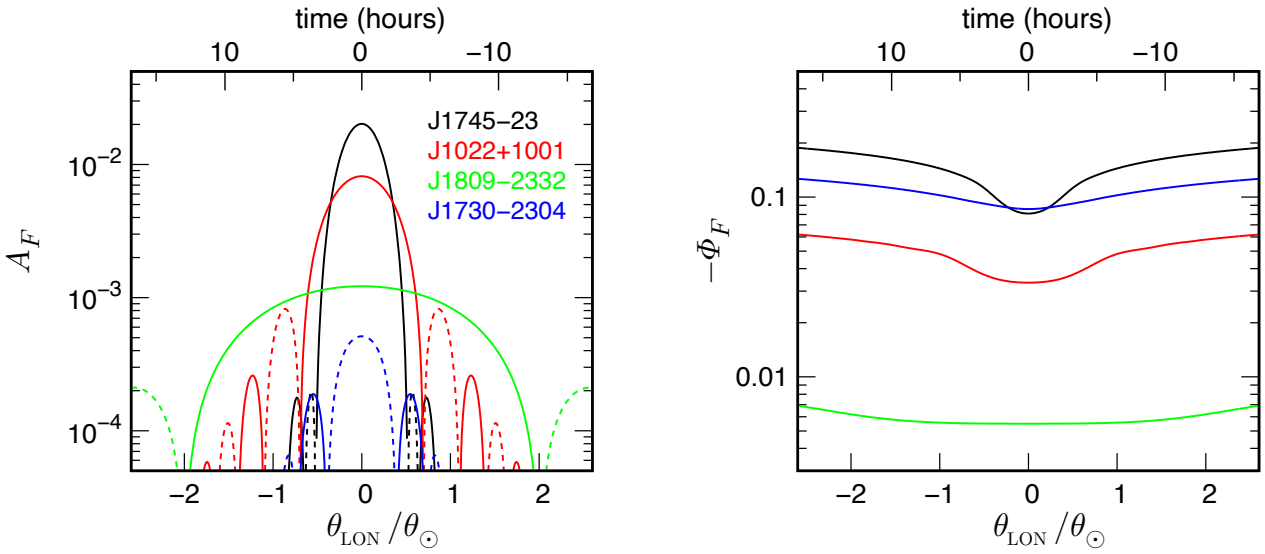

FIG. 7.— Amplitude and phase modulations of the four pulsars moving behind the Sun. The lower x axis is the pulsar position $\theta_{\rm LON}/\theta_\odot$ along the ecliptic longitude (Fig.6), while the upper x axis represents the corresponding crossing time. Dotted curves in the left panel represent negative values.

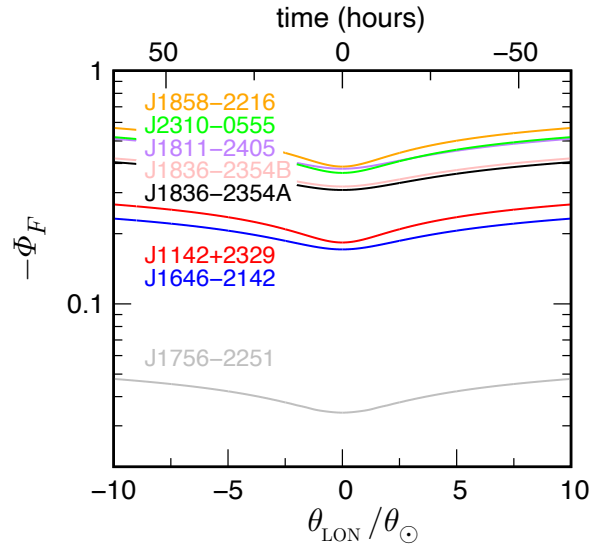

FIG. 8.— Phase modulations of the eight pulsars passing close to (but not behind) the Sun.

parameters are normalized by the SNR. Therefore, the results do not depend on a specific form of S_n. In the second equality of Eq. (17), we neglect A_F and use the approximation $\cos^2(2\pi ft+\phi_0+\Phi_F)\simeq 1/2$ obtained by long-time averaging.

The lensed waveform (16) depends on the solar density profile, the constant amplitude h_0, and the constant phase ϕ_0. Let the solar density profile be characterized by N parameters $A_{\rm i}$ (i $=1,2,\cdots,N$). The total set of fitting parameters is $p_\mu=(A_{\rm i},\ln h_0,\phi_0)$ with $\mu=1,2,\cdots,N+2$. The measurement accuracy of p_μ is given by the inverse of the Fisher matrix: $\Delta p_\mu=[(\Gamma^{-1})_{\mu\mu}]^{1/2}$. Neglecting the degeneracy with the other parameters, $\Delta p_\mu=(\Gamma_{\mu\mu})^{-1/2}$. The Fisher matrix is given by (Finn 1992; Cutler & Flanagan 1994)

$$\Gamma_{\mu\nu}=\frac{1}{S_n(f)}\int_{-T/2}^{T/2}dt\,\frac{\partial h^{\rm L}(t;f)}{\partial p_\mu}\frac{\partial h^{\rm L}(t;f)}{\partial p_\nu}. \tag{18}$$

Using Eqs. (16) and (17), all components of Γ are given as follows:

$$\begin{aligned}
\Gamma_{A_{\rm i}A_{\rm j}}&=\int_t\left[\frac{\partial A_F(t;f)}{\partial A_{\rm i}}\frac{\partial A_F(t;f)}{\partial A_{\rm j}}\right.\\
&\qquad\left.+\{1+A_F(t;f)\}^2\,\frac{\partial\Phi_F(t;f)}{\partial A_{\rm i}}\frac{\partial\Phi_F(t;f)}{\partial A_{\rm j}}\right],\\
\Gamma_{A_{\rm i}\ln h_0}&=\int_t\{1+A_F(t;f)\}\,\frac{\partial A_F(t;f)}{\partial A_{\rm i}},\\
\Gamma_{A_{\rm i}\phi_0}&=\int_t\{1+A_F(t;f)\}^2\,\frac{\partial\Phi_F(t;f)}{\partial A_{\rm i}},\\
\Gamma_{\ln h_0\ln h_0}&=\Gamma_{\phi_0\phi_0}=\int_t\{1+A_F(t;f)\}^2,\\
\Gamma_{\ln h_0\phi_0}&=0,
\end{aligned} \tag{19}$$

with

$$\int_t\equiv{\rm SNR}^2\,\frac{1}{T}\int_{-T/2}^{T/2}dt.$$

Similarly to Eq. (17), we here applied the approximations $\sin^2$ or $\cos^2(2\pi ft+\phi_0+\Phi_F)\simeq 1/2$ and $\sin(2\pi ft+\phi_0+\Phi_F)\,\cos(2\pi ft+\phi_0+\Phi_F)\simeq 0$. From Eq. (19), Δp_μ simply scales as $\Delta p_\mu\propto{\rm SNR}^{-1}$.

The simple waveform (14) neglects the detector response which depends on other source parameters such the inclination of the spin axis and GW polarization. Owing to Earth's spin and orbital motion, the detector response causes daily and yearly periodic modulations on both amplitude and phase. Unlike the solar modulation (which is temporary but repeats annually), the response modulations are trigonometric functions of time. We expect that the solar modulation can be distinguishable from the response modulations and thus the response

does not significantly affect the measurement accuracies of the solar model parameters.

4.2. *Constraint on the potential amplitude*

This subsection presents the measurement accuracy of the overall amplitude of the solar gravitational potential. Replacing the potential as

$$\hat{\psi}(\theta) \to A_\psi \hat{\psi}(\theta), \tag{20}$$

we calculate the measurement error in A_ψ. The derivatives in the Fisher matrix with respect to A_ψ are numerically obtained by changing A_ψ by $\pm 1\,\%$.

Figure 9 plots the measurement accuracies of A_ψ, $\ln h_0$ and ϕ_0 for the pulsars moving behind the Sun at $f > 100\,\mathrm{Hz}$. The results are normalized with $\mathrm{SNR} = 100$ over a one-year observation period. Because $|A_F| \ll |\Phi_F|$, A_ψ is mainly determined by the phase modulation. The slope of ΔA_ψ changes slightly at the surface (corresponding to $T \approx 10^{-3}\,\mathrm{yr}$); the slope is steeper (shallower) inside (outside) the Sun. These results can be explained as follows. In the Sun's interior, $|\Phi_F|$ increases with θ (in contrast to the constant ϕ_0), thus A_ψ and ϕ_0 can be determined almost independently. Outside the Sun, Φ_F is nearly constant at large $\theta\,(\gg \theta_\odot)$, thus A_ψ and ϕ_0 are degenerate to some extent. The dashed red curve plots ΔA_ψ without parameter degeneracy (i.e., $\Delta A_\psi = (\Gamma_{A_\psi A_\psi})^{-1/2}$), which is ~ 10 times better than the solid red curve. Previously, Marchant et al. (2020) roughly estimated the detectability of lensing signatures. As they ignored the parameter degeneracy, they underestimated the measurement error. Inside the Sun, h_0 cannot be determined because h_0 and A_F are highly degenerate, but outside the Sun, the degeneracy is broken and $\Delta \ln h_0 \simeq \mathrm{SNR}^{-1}$.

We caution that $\Delta\phi_0$ shown in Fig. 9 depends on the arbitrary constant in the gravitational potential. If a constant term is added to the potential, i.e., $\hat{\psi}(\theta) \to \hat{\psi}(\theta) + \hat{\psi}_0$, the phase modulation changes as $\Phi_F \to \Phi_F - 2\pi f\hat{\psi}_0/c^3$ using Eqs. (1)–(3). Two components of the Fisher matrix change accordingly[6]. After some algebra, one finds that ΔA_ψ, $\Delta \ln h_0$, and $(\Gamma^{-1})_{A_\psi \ln h_0}$ are independent of $\hat{\psi}_0$ but $\Delta\phi_0$ and its cross correlations, $(\Gamma^{-1})_{A_\psi \phi_0}$ and $(\Gamma^{-1})_{\ln h_0 \phi_0}$, do depend on $\hat{\psi}_0$.

Table 2 lists the ΔA_ψ results of all pulsars. Although ΔA_ψ varies among the pulsars, $f\Delta A_\psi$ is almost constant; i.e., it is independent of the impact parameter to the Sun. ΔA_ψ can then be approximately fitted as

$$\Delta A_\psi \approx 0.3 \left(\frac{f}{300\,\mathrm{Hz}}\right)^{-1} \left(\frac{\mathrm{SNR}}{100}\right)^{-1}, \tag{21}$$

indicating that a higher-frequency pulsar is more promising for detecting A_ψ. According to Eq. (21), A_ψ can be detected at the 3σ confidence level when $\mathrm{SNR} \approx 100\,(f/300\mathrm{Hz})^{-1}$.

4.3. *Measurement of the solar density profile*

[6] $\Gamma_{A_\psi \phi_0} \to \Gamma_{A_\psi \phi_0} - (2\pi f\hat{\psi}_0/c^3)\Gamma_{\phi_0\phi_0}$ and $\Gamma_{A_\psi A_\psi} \to \Gamma_{A_\psi A_\psi} - (4\pi f\hat{\psi}_0/c^3)\Gamma_{A_\psi \phi_0} + (2\pi f\hat{\psi}_0/c^3)^2\Gamma_{\phi_0\phi_0}$.

TABLE 2
Measurement accuracies of the potential amplitude A_ψ (the fiducial value = 1) over one year of observation with $\mathrm{SNR} = 100$.

name	ΔA_ψ	$f\Delta A_\psi$ (Hz)
J1745−23	0.24 (0.026)	90
J1022+1001	0.74 (0.077)	90
J1809−2332	6.6 (0.69)	90
J1730−2304	0.37 (0.038)	91
J1858-2216	0.11 (0.011)	92
J1142+0119	0.23 (0.024)	92
J2310-0555	0.12 (0.012)	92
J1756-2251	1.3 (0.13)	92
J1646-2142	0.27 (0.028)	93
J1811-2405	0.12 (0.013)	93
J1836-2354B	0.16 (0.016)	93
J1836-2354A	0.15 (0.015)	93

Note. — Values in parentheses are calculated without parameter degeneracy.

TABLE 3
Measurement accuracies of the density amplitudes in two annuli over a one-year observation period with $\mathrm{SNR} = 10^4$.

name	Case (I) $\Delta A_{\Sigma 1,2}$	Case (II) $\Delta A_{\Sigma 1}$, $\Delta A_{\Sigma 2}$
J1745−23	0.40	0.11, 1.8
J1022+1001	2.0	0.47, 8.0
J1730−2304	2.9	1.3, 22

Note. — In Case (I), $\Delta A_{\Sigma 1} = \Delta A_{\Sigma 2}$.

TABLE 4
Same as Table 3, but for three annuli and a one-year observation period with $\mathrm{SNR} = 10^5$.

name	Case (I) $\Delta A_{\Sigma 1}$, $\Delta A_{\Sigma 2}$, $\Delta A_{\Sigma 3}$	Case (II) $\Delta A_{\Sigma 1}$, $\Delta A_{\Sigma 2}$, $\Delta A_{\Sigma 3}$
J1745−23	0.24, 0.33, 0.10	0.029, 0.24, 1.5
J1022+1001	1.3, 1.8, 0.53	0.17, 1.3, 6.9
J1730−2304	0.43, 0.92, 0.74	0.22, 0.93, 6.3

This subsection presents our main result, namely, the measurement accuracy of the solar density profile. Let the surface density be divided into N annuli (Fig. 10), where N is 2 or 3. We write the surface mass density of the i-th annulus as $\Sigma_\mathrm{i}(\theta)$ and the mass as M_i ($\mathrm{i} = 1, \cdots, N$), where a smaller i corresponds to an inner annulus. We consider the following two cases:

Case (I): Each annulus has the same mass ($= M_\odot/N$).

Case (II): Each annulus has the same radial thickness ($= \theta_\odot/N$).

In Case (I), the boundary radius between the annuli is $0.20\,\theta_\odot$ for $N = 2$. The boundary radii are $0.14\,\theta_\odot$ and $0.26\,\theta_\odot$ between annulus 1 and 2 and between annulus 2 and 3, respectively, for $N = 3$. In Case (II), the mass ratios are $M_1 : M_2 \simeq 17 : 1$ for $N = 2$ and $M_1 : M_2 : M_3 \simeq 57 : 13 : 1$ for $N = 3$ (i.e., the mass reduces from the innermost to the outermost annulus).

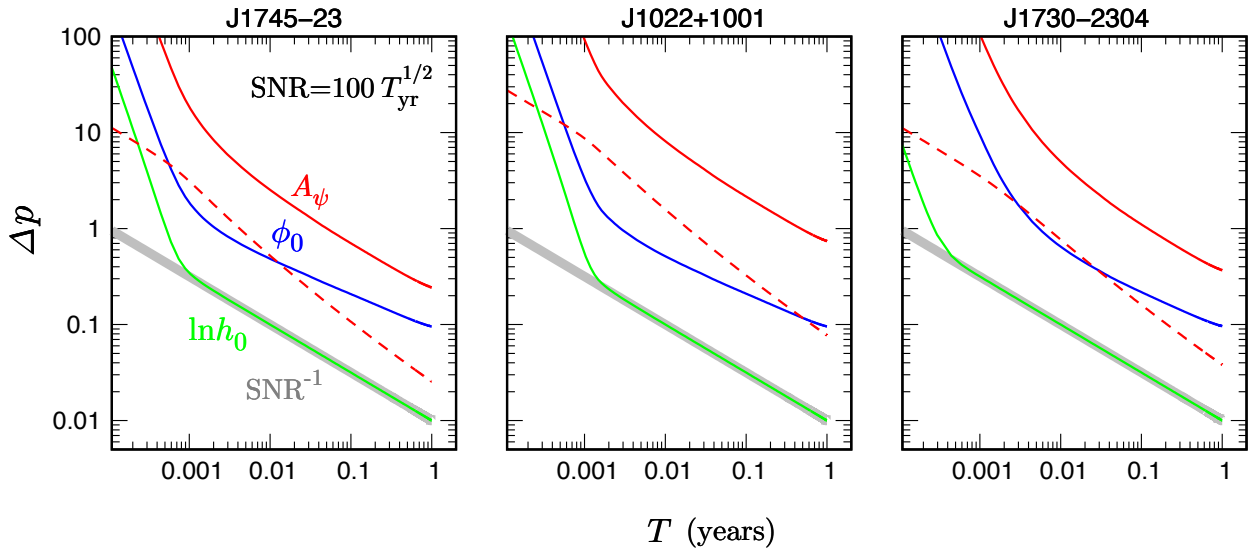

FIG. 9.— Measurement accuracies of the solar-potential amplitude A_ψ defined in Eq.(20), the amplitude h_0, and phase ϕ_0 of the pulsars crossing behind the Sun. Dashed red curve plots ΔA_ψ neglecting the parameter degeneracy. The horizontal axis T denotes the observational period. The signal-to-noise ratio (SNR) is set to $100\,(T/\mathrm{yr})^{1/2}$ and the results simply scale as $\Delta p \propto \mathrm{SNR}^{-1}$. Thick gray line denotes SNR^{-1}.

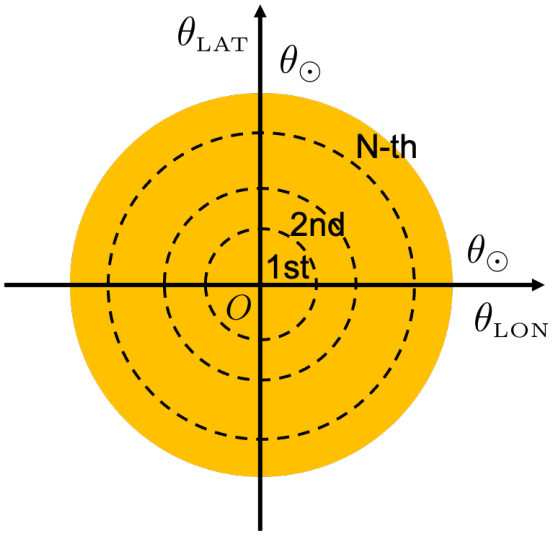

FIG. 10.— Division of the solar surface into N annuli. Each annulus has the same mass in Case (I) and the same radial width in Case (II).

We change the amplitude of the i-th density as

$$\Sigma_{\rm i}(\theta) \to A_{\Sigma{\rm i}}\Sigma_{\rm i}(\theta), \tag{22}$$

while fixing the total mass, i.e., $\sum_{\rm i=1}^{N} A_{\Sigma{\rm i}} M_{\rm i} = M_\odot$. Under these settings, we calculate the measurement accuracies of $A_{\Sigma{\rm i}}$, $\ln h_0$, and ϕ_0. When $N = 2$, the density profile is solely characterized by the fitting parameter $A_{\Sigma1}$ because the total mass is fixed, i.e., $M_1\Delta A_{\Sigma1} = M_2\Delta A_{\Sigma2}$. Similarly, when $N = 3$, the fitting parameters are $A_{\Sigma1}$ and $A_{\Sigma2}$. The other parameter, $\Delta A_{\Sigma3}$, is determined via $(M_3\Delta A_{\Sigma3})^2 = (M_1\Delta A_{\Sigma1})^2 + (M_2\Delta A_{\Sigma2})^2 + 2M_1M_2(\Gamma^{-1})_{A_{\Sigma1}A_{\Sigma2}}$. To obtain the derivative with respect to $A_{\Sigma{\rm i}}$ in the Fisher matrix, we numerically calculate the derivatives of the potential in Eq. (4) and the amplification factor in Eq. (6) by changing $A_{\Sigma{\rm i}}$ by $\pm1\,\%$.

Figure 11 plots the measurement accuracies of $A_{\Sigma{\rm i}}$ for $N = 2$. As the total mass is fixed, the lensed signal is insensitive to the density profile when the pulsar is outside the Sun. Therefore, the accuracies are not improved at $T \gtrsim 10$ hours. J1745-23 gives the best accuracy because it has the highest frequency and smallest impact parameter. J1730-2304 has a higher frequency than J1022+1001 but its larger impact parameter lessens the constraint. In Case (II), $\Delta A_{\Sigma2}$ is 17 times larger than $\Delta A_{\Sigma1}$, reflecting the mass ratio $M_1/M_2 \simeq 17$. According to the figure, at least $\mathrm{SNR} \approx 10^4\,(T/\mathrm{yr})^{1/2}$ is required for probing the solar density profile, but a lower SNR may be sufficient for probing with J1745-23. We comment that $\Delta \ln h_0$ and $\Delta\phi_0$ agree with SNR^{-1} outside the Sun (corresponding to $T > 10$ hours, these results are not plotted in the figure). The numerical values of $\Delta A_{\Sigma{\rm i}}$ are listed in Table 3.

Figure 12 plots the measurement accuracies of $A_{\Sigma{\rm i}}$ for $N = 3$. In Case (I), $\Delta A_{\Sigma3}$ shows the highest accuracy for most pulsars (the exception is J1730-2304) because the third annulus (with radius ranging from $0.26\,\theta_\odot$ to $\theta_\odot$) has the largest area. Therefore, the pulsar remains longer in the third annulus than in the other annuli. In Case (II), $\Delta A_{\Sigma1} < \Delta A_{\Sigma2} < \Delta A_{\Sigma3}$ simply because the inner annulus is more massive than the outer one. The numerical values of $\Delta A_{\Sigma{\rm i}}$ are listed in Table 4. According to Fig. 12, at least $\mathrm{SNR} \approx 10^5\,(T/\mathrm{yr})^{1/2}$ is required for measuring the density profile with $N = 3$. The SNR must be further increased for larger N (> 3).

In geometrical optics, Φ_F is fully determined by the mass enclosed within a given radius. Therefore, a pulsar can probe the enclosed mass down to the impact parameter. In wave optics, Φ_F also depends on the outer density profile owing to diffraction (Subsection 2.3). Therefore, the accuracy of $A_{\Sigma{\rm i}}$ depends on the frequency and impact parameter in a complicated manner. Combining the

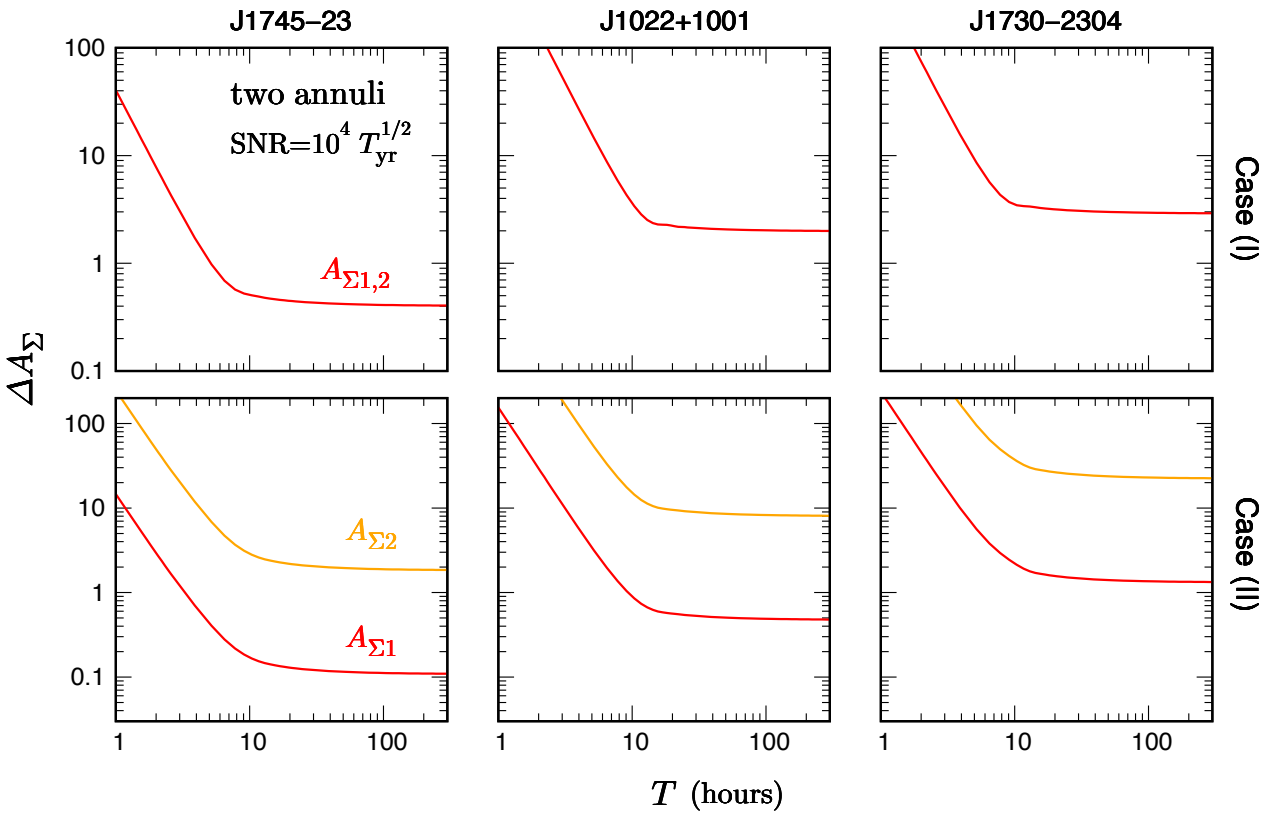

FIG. 11.— Measurement accuracies of the solar-density amplitudes in the i-th annulus $A_{\Sigma i}$ for the pulsars crossing behind the Sun. Upper and lower panels plot the results in Case (I) and (II), respectively. In the upper panels, $\Delta A_{\Sigma1} = \Delta A_{\Sigma2}$. The horizontal axis T denotes the observational period. SNR is set to $10^4\,(T/\mathrm{yr})^{1/2}$ and the results simply scale as $\Delta A_{\Sigma i} \propto \mathrm{SNR}^{-1}$.

results of different pulsars improves the measurement accuracy of the solar density and increases the radial range of the estimation.

Figures 11 and 12 suggest that the accuracies strongly depend on the chosen boundary. In Case (I), the accuracies are similar in different annuli but in Case (II), the accuracy is better in the inner annulus. This implies that the annulus mass mainly determines the accuracy. The boundary that maximizes the accuracy will depend on the frequency and impact parameter of the pulsar.

The strain sensitivities of the planned detectors of Cosmic Explorer (CE)[7] and Einstein Telescope (ET)[8] will be approximately 100 times better than those of the LIGO O3 run. The current upper limits in Table 1 were determined from observations taken over approximately one year in the O3 run. These limits correspond to an upper limit of SNR $\lesssim 10$ (Appendix C of Abbott et al. 2019). Therefore, in CE and ET observations, the best SNR for these known pulsars is estimated as $\approx 10^3\,(T/\mathrm{yr})^{1/2}$ (a similar discussion is given in Section V of Marchant et al. 2020). Judging from these estimates, measuring the density profile using these pulsars will be a difficult task in the near future. To alleviate this problem, we require more pulsars than those detected by radio telescopes to date (as discussed in the next section). Moreover, these pulsars must have high frequencies and small impact parameters.

[7] https://cosmicexplorer.org/
[8] https://www.et-gw.eu/

TABLE 5
GLOBULAR CLUSTERS CROSSING BEHIND THE SUN

name	$\theta_{\rm LAT}/\theta_\odot$	$\theta_{\rm h}/\theta_\odot$	$D_{\rm s}$ (kpc)	mass ($M_\odot$)
NGC 6287	0.49	0.046	7.9	1.5×10^5
NGC 6717	0.50	0.043	7.5	3.6×10^4
NGC 6642	−0.89	0.046	8.1	3.4×10^4

NOTE. — Listed are the ecliptic latitude of the cluster center $\theta_{\rm LAT}$, the half-light angular radius $\theta_{\rm h}$, the distance $D_{\rm s}$, and the mass. Here, the distance and mass are taken from Baumgardt's catalog of globular clusters[a] (e.g., Baumgardt & Hilker 2018).

[a] https://people.smp.uq.edu.au/HolgerBaumgardt/globular/

5. MILLISECOND PULSARS

This section roughly estimates the number of MSPs moving behind the Sun that will be found in the near future.

The present ATNF catalog lists approximately 3300 pulsars, including around 500 highly spinning pulsars with a spin period of $< 10\,\mathrm{ms}$ (corresponding to $f > 200\,\mathrm{Hz}$). These pulsars are the so-called MSPs. The Milky Way is estimated to host 40000–90000 MSPs (e.g., Bhattacharyya & Roy 2022). As the sky fraction of the zodiac belt swept by the Sun is $2\pi \times 2\theta_\odot/(4\pi) \simeq 0.5\%$, the belt probably holds 200–400 MSPs. Almost none of these MSPs have been found, but tens of them will be identified in ongoing and upcoming radio surveys. For instance, the Canadian Hydrogen Intensity Mapping Ex-

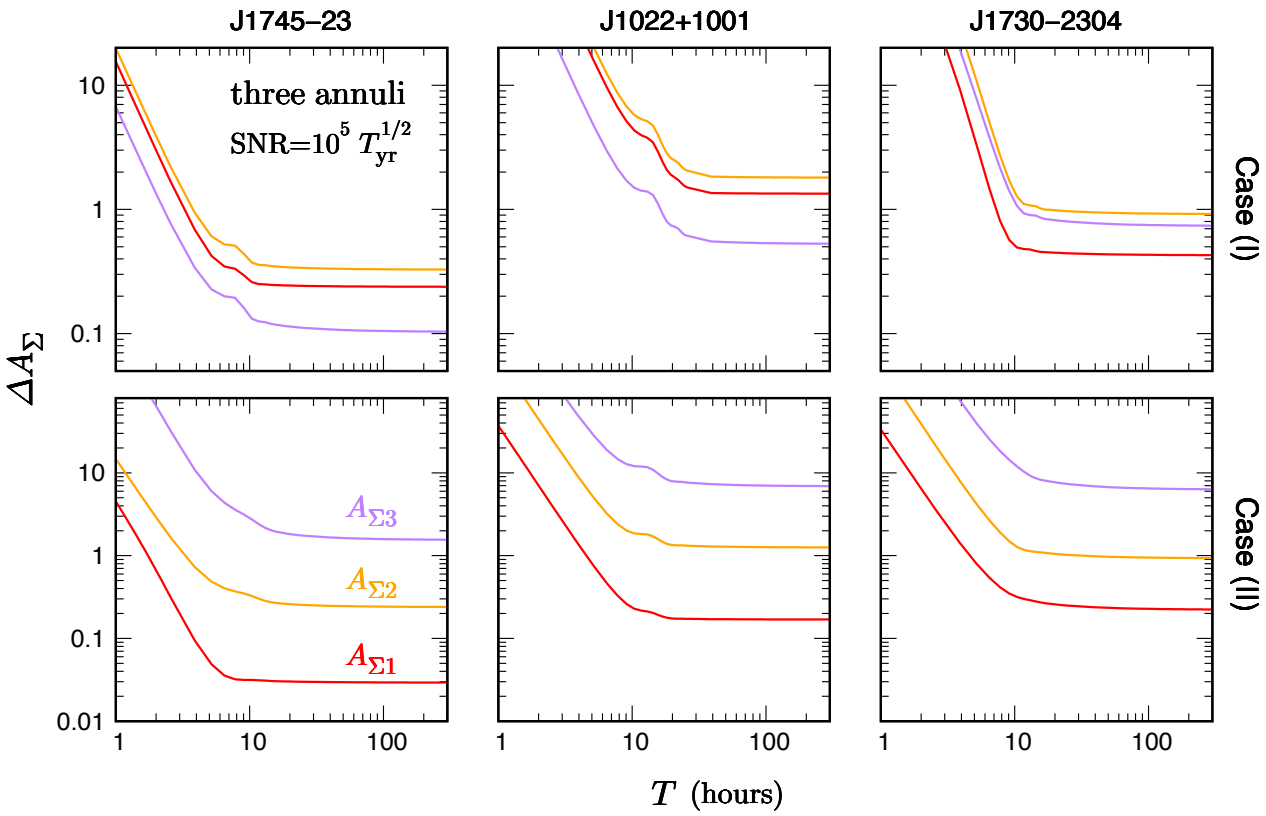

FIG. 12.— Same as Fig. 11, but for three annuli with SNR $= 10^5\,(T/\mathrm{yr})^{1/2}$.

periment (CHIME)[9], MeerKAT[10] and the Five-hundred-meter Aperture Spherical radio Telescope (FAST)[11] will detect ≈ 1000 MSPs over the sky (Lorimer et al. 2019, their Table 1). These performances will be surpassed by the Square Kilometer Array, which will detect 1500 MSPs in phase 1 (Keane et al. 2015).

At present, approximately 220 MSPs have been found in 33 globular clusters[12]; ~ 7 MSPs per cluster on average. Per unit mass, pulsars are two or three orders of magnitudes more abundant in clusters than in the Galactic disk (Freire 2013). Therefore, many MSPs probably exist in clusters. Among the 157 clusters listed in the McMaster catalog of Milky Way globular clusters[13] (version 2010, Harris 1996, 2010), three globular clusters move behind the Sun. The data are summarized in Table 5. Although no MSPs have been discovered in these clusters[14], tens of MSPs are expected in each cluster.

6. CONCLUSIONS

We studied the detectability of the solar density profiling using GW lensing with known pulsars. After selecting suitable pulsars with high frequencies and small impact parameters to the Sun from the ATNF catalog, we calculated the measurement accuracy of the overall amplitude of the solar gravitational potential using a Fisher analysis. The lensing signature can be detected with 3σ confidence when SNR $\approx 100\,(f/300\,\mathrm{Hz})^{-1}$ during one year of observations. The detection is therefore improved with high-frequency pulsars. The signature can be detected even if the pulsar trajectory does not pass behind the Sun (in such cases, the impact parameter to the Sun does not significantly affect the detectability). We found that the detectability is degraded by parameter degeneracy with the constant phase of waveform. Next, we divided the projected density profile into two or three annuli, and calculated the measurement accuracy of each annulus mass. If three known pulsars move behind the Sun with $f > 100\,\mathrm{Hz}$, a high SNR ($\gtrsim 10^4$) in a year long observation is required for measuring the density profile in the two-annulus case. The SNR must be raised to $\gtrsim 10^5$ in the three-annulus case.

Currently, only two known MSPs move behind the Sun, but 200–400 can potentially exist within our Galaxy. Ongoing and future radio surveys such as SKA, CHIME, and FAST will find tens of these MSPs in coming decades.

The solar density profile has been already measured to percent level precision based on global helioseismology (a recent review by Basu 2016). GW lensing will likely become a complementary and independent method for probing the Sun in future.

[9] https://chime-experiment.ca/en
[10] https://www.sarao.ac.za/gallery/meerkat/
[11] https://fast.bao.ac.cn
[12] http://www.naic.edu/ pfreire/GCpsr.html
[13] Data may be downloaded from https://physics.mcmaster.ca/Fac_Harris/mwgc.dat
[14] http://www.naic.edu/ pfreire/GCpsr.html

ACKNOWLEDGMENTS

We thank Hideyuki Hotta for his useful comment on helioseismology. We thank the CASS (CSIRO (Commonwealth Scientific and Industrial Research Organisa-

tion) Astronomy and Space Science) pulsar group for developing and maintaining the ATNF pulsar catalog. This work is supported in part by MEXT Japan and JSPS KAKENHI Grant Numbers of JP22H00130 (RT), JP20H05855 (RT), JP17H06359 (TS), JP21H05453 (TS), and JP19K03864 (TS).

REFERENCES

Abbott, B. P., Abbott, R., Abbott, T. D., et al. 2016, Phys. Rev. Lett., 116, 061102
—. 2017, ApJ, 839, 12
—. 2019, ApJ, 879, 10
Abbott, R., Abe, H., Acernese, F., et al. 2022a, Phys. Rev. D, 106, 042003
Abbott, R., Abbott, T. D., Abraham, S., et al. 2021, Phys. Rev. D, 103, 064017
Abbott, R., Abe, H., Acernese, F., et al. 2022b, ApJ, 935, 1
Abdo, A. A., Ackermann, M., Ajello, M., et al. 2009, Science, 325, 840
Backer, D. C., & Hellings, R. W. 1986, ARA&A, 24, 537
Bahcall, J. N., Serenelli, A. M., & Basu, S. 2005, ApJ, 621, L85
Bartelmann, M., & Schneider, P. 2001, Phys. Rep., 340, 291
Basu, S. 2016, Living Reviews in Solar Physics, 13, 2
Baumgardt, H., & Hilker, M. 2018, MNRAS, 478, 1520
Bhattacharyya, B., & Roy, J. 2022, Astrophysics and Space Science Library, 465, 1
Bliokh, P. V., & Minakov, A. A. 1975, Ap&SS, 34, L7
Bontz, R. J., & Haugan, M. P. 1981, Ap&SS, 78, 199
Cameron, A. D., Champion, D. J., Bailes, M., et al. 2020, MNRAS, 493, 1063
Camilo, F., Nice, D. J., Shrauner, J. A., & Taylor, J. H. 1996, ApJ, 469, 819
Choi, H. G., Park, C., & Jung, S. 2021, Phys. Rev. D, 104, 063001
Cutler, C., & Flanagan, É. E. 1994, Phys. Rev. D, 49, 2658
Cyranski, J. F., & Lubkin, E. 1974, Annals of Physics, 87, 205
Dai, L., Li, S.-S., Zackay, B., Mao, S., & Lu, Y. 2018, Phys. Rev. D, 98, 104029
Dalang, C., Cusin, G., & Lagos, M. 2022, Phys. Rev. D, 105, 024005
Edwards, R. T., Hobbs, G. B., & Manchester, R. N. 2006, MNRAS, 372, 1549
Ezquiaga, J. M., Holz, D. E., Hu, W., Lagos, M., & Wald, R. M. 2021, Phys. Rev. D, 103, 064047
Faulkner, A. J., Stairs, I. H., Kramer, M., et al. 2004, MNRAS, 355, 147
Ferdman, R. D., Stairs, I. H., Kramer, M., et al. 2014, MNRAS, 443, 2183
Finn, L. S. 1992, Phys. Rev. D, 46, 5236
Freire, P. C. C. 2013, Neutron Stars and Pulsars: Challenges and Opportunities after 80 years, 291, 243
Glampedakis, K., & Gualtieri, L. 2018, Astrophysics and Space Science Library, 457, 673
Guo, X., & Lu, Y. 2020, Phys. Rev. D, 102, 124076
Harris, W. E. 1996, AJ, 112, 1487
—. 2010, arXiv:1012.3224
Hobbs, G. B., Edwards, R. T., & Manchester, R. N. 2006, MNRAS, 369, 655
Hou, S., Fan, X.-L., & Zhu, Z.-H. 2019, Phys. Rev. D, 100, 064028
Jung, S., & Kim, S. 2022, arXiv:2210.02649
Keane, E., Bhattacharyya, B., Kramer, M., et al. 2015, Advancing Astrophysics with the Square Kilometre Array (AASKA14), 40
Keith, M. J., Jameson, A., van Straten, W., et al. 2010, MNRAS, 409, 619
Liao, K., Biesiada, M., & Zhu, Z.-H. 2022, Chinese Physics Letters, 39, 119801
Lorimer, D., Pol, N., Rajwade, K., et al. 2019, BAAS, 51, 261
Lorimer, D. R., Nicastro, L., Lyne, A. G., et al. 1995, ApJ, 439, 933
Lynch, R. S., Ransom, S. M., Freire, P. C. C., & Stairs, I. H. 2011, ApJ, 734, 89
Macquart, J. P. 2004, A&A, 422, 761
Manchester, R. N., Hobbs, G. B., Teoh, A., & Hobbs, M. 2005, AJ, 129, 1993
Marchant, P., Breivik, K., Berry, C. P. L., Mandel, I., & Larson, S. L. 2020, Phys. Rev. D, 101, 024039
Nakamura, T. T. 1998, Phys. Rev. Lett., 80, 1138
Nakamura, T. T., & Deguchi, S. 1999, Progress of Theoretical Physics Supplement, 133, 137
Ng, C., Guillemot, L., Freire, P. C. C., et al. 2020, MNRAS, 493, 1261
Nice, D., Demorest, P., Stairs, I., et al. 2015, Tempo: Pulsar timing data analysis, Astrophysics Source Code Library, record ascl:1509.002
Oguri, M. 2019, Reports on Progress in Physics, 82, 126901
Oguri, M., & Takahashi, R. 2020, ApJ, 901, 58
Ohanian, H. C. 1974, International Journal of Theoretical Physics, 9, 425
Patla, B., & Nemiroff, R. J. 2008, ApJ, 685, 1297
Ray, P. S., Kerr, M., Parent, D., et al. 2011, ApJS, 194, 17
Ray, P. S., Abdo, A. A., Parent, D., et al. 2012, arXiv:1205.3089
Reardon, D. J., Shannon, R. M., Cameron, A. D., et al. 2021, MNRAS, 507, 2137
Riles, K. 2022, arXiv:2206.06447
Roy, J., & Bhattacharyya, B. 2013, ApJ, 765, L45
Sanpa-Arsa, S. 2016, PhD thesis, University of Virginia
Schneider, P., Ehlers, J., & Falco, E. E. 1992, Gravitational Lenses, 112
Sonnabend, D. 1979, PhD thesis, Stanford University, California
Takahashi, R. 2004, A&A, 423, 787
—. 2006, ApJ, 644, 80
Takahashi, R., & Nakamura, T. 2003, ApJ, 595, 1039
The LIGO Scientific Collaboration, the Virgo Collaboration, the KAGRA Collaboration, et al. 2021, arXiv:2111.03606
—. 2022, arXiv:2201.00697
Yao, J. M., Manchester, R. N., & Wang, N. 2017, ApJ, 835, 29